

PSFC/JA-06-6

**Energy deposition of MeV electrons in
compressed targets of fast-ignition
inertial confinement fusion**

C. K. Li and R. D. Petrasso

1 April 2006

Plasma Science and Fusion Center
Massachusetts Institute of Technology
Cambridge, MA 02139 USA

This work was supported in part by U.S. Department of Energy Contract #DE-FG03-99SF21782, LLE subcontract #PO410025G, LLNL subcontract #B313975, and the Fusion Science Center for Extreme States of Matter and Fast Ignition Physics at University of Rochester.

Accepted and to be published in *Physics of Plasmas*

Energy deposition of MeV electrons in compressed targets of fast-ignition inertial confinement fusion

C. K. Li and R. D. Petrasso

*Plasma Science and Fusion Center, Massachusetts Institute of Technology,
Cambridge, MA 02139*

ABSTRACT

Energy deposition of MeV electrons in dense plasmas, critical for fast ignition in inertial confinement fusion (ICF), is modeled analytically. It is shown that classical stopping and scattering dominate electron transport and energy deposition when the electrons reach the dense plasmas in the cores of compressed targets, while “anomalous” stopping associated with self-generated fields and micro instabilities (suggested by previous simulations) might initially play an important role in the lower-density plasmas outside the dense core. We calculate the energy deposition of MeV electrons in pre-compressed deuterium-tritium (DT) fast-ignition targets, rigorously treating electron energy loss from scattering, longitudinal straggling and transverse blooming. We demonstrate that, while the initial penetration of electrons in a compressed target results in approximately uniform energy deposition, the latter stages involve mutual couplings of energy loss, straggling, and blooming that lead to enhanced, non-uniform energy deposition. These results are critically important for quantitatively assessing ignition requirements for fast ignition.

Email: li@psfc.mit.edu

I. INTRODUCTION

Fast ignition,¹ an alternative approach to inertial confinement fusion (ICF), has recently attracted significant attention. In this scheme, different from the conventional approach to central hot-spot ignition, a pre-compressed deuterium-tritium (DT) target will be ignited by an external “spark”. Since it separates capsule compression from hot spot formation, fast ignition may potentially relax the conditions on target compression and reduce the total energy requirements for ICF ignition, leading to higher target gain.¹⁻³

Successful realization of fast ignition requires understanding and controlling of the transport and energy deposition of MeV electrons in the target. Energetic electrons are generated by an ultrahigh-intensity ($\geq 10^{18}$ W/cm²), short-pulse ($\leq 10^{-12}$ s) laser interacting at the critical surface of a pre-compressed target. During a time period of ~ 10 ps, a total energy ~ 10 kJ needs to be delivered to the compressed core; fast ignition then occurs in response to electron energy deposition, with DT alphas bootstrapping a fusion burn wave that propagates to the surrounding dense fuel.¹⁻³

As illustrated schematically in Fig. 1, the generated electron beam is typically characterized by a radius ~ 10 μm and current $\geq 3 \times 10^8$ A. As it propagates over a distance ~ 100 μm to the core, such an electron beam experiences a tremendous dynamic range of plasma conditions, from the initial critical surface ($n_c \sim 10^{21}/\text{cm}^3$) to the highly compressed core ($n_e \sim 10^{26}/\text{cm}^3$). Return currents and associated self fields are generated.¹⁻³ Numerical simulations⁴⁻⁶ suggest that the electron transport is highly filamented due to self fields and microscopic instabilities,⁷ which occur at early times when beam density, n_b , is comparable to or larger than the critical density n_c . In these simulations plasma heating is dominated by “anomalous” stopping which may be largely characterized by collective beam stopping, possibly due to coalescence of current filaments and related ion dynamics. Return-current Ohmic heating also plays an important role due to the relatively low plasma temperature.³ Subsequently, however, as these electrons enter the dense plasma region where $n_b/n_e \ll 1$ and plasma $T_e \sim \text{keV}$,^{8,9} classical Coulomb collisions will dominate electron transport and energy deposition (as will be discussed in the next section).

This paper is organized as follows. Section II discusses interaction regimes for MeV electrons in dense plasmas. An analytic model, which links electron energy loss

with range straggling and beam blooming, is presented in Section III. Section IV discusses some fundamental dependences and consequences of these calculations, while Section V summarizes our major results.

II. ELECTRON TRANSPORT AND ENERGY DEPOSITION IN THE DENSE CORE

While numerical simulations have suggested that microscopic instabilities and anomalous stopping might initially play an important role in the outer region of low-density plasma, we argue that the interaction of the electrons with dense plasma in the core is dominated by classical Coulomb collisions and that the effects of scattering will ultimately determine the electron transport and energy deposition.^{8,9} To illustrate this, we consider a 1-MeV electron beam (beam radius $r_b=10 \mu\text{m}$) in a compressed DT target ($\rho=300 \text{ g/cm}^3$ and $T_e=5 \text{ keV}$). The maximum field $B_{\text{max}}=\mu_0 I_b/(2\pi r_b)$ occurs at the beam surface, where

$$I_b = n_b e v \pi r_b^2 = \frac{\varepsilon_b(\text{kJ})}{E(\text{MeV})t_b(\text{ps})} \times 10^9 (\text{Amp}) \quad (1)$$

is the beam current calculated in terms of electron energy E , beam energy ε_b , and the beam pulse duration t_b .

Relevant to fast ignition ($E=1 \text{ MeV}$ and $t_b =10 \text{ ps}$), Fig. 2 plots the I_b and associated B_{max} as a function of the beam energy. For example, for ignition energy $\varepsilon_b=15 \text{ kJ}$, $I_b \sim 10^9 \text{ A}$ and $B_{\text{max}} \sim 10^{11} \text{ Gauss}$ are expected. The maximum electron gyro radius (r_g) associated to B_{max} is $r_g(\text{cm}) = v m_e c / e B = 2.38 \times 10^3 \sqrt{E(\text{MeV})} / B(\text{Gauss})$. Figure 3 shows r_g as a function of beam energy for different beam radii; it is consistently larger than plasma Debye length λ_D . This suggests that an electron does not feel the magnetic field locally but is subjected to Coulomb collisions. In addition, while $\omega_{ce}\tau \gg 1$ in this region, one has $L_{||} \gg \lambda$ and $L_{\perp} \gg \sqrt{\lambda r_g}$ (ω_{ce} is the electron gyro frequency; $\lambda=v\tau$ is the mean free path and τ is the collision time; $L_{||}$ is the longitudinal plasma scale length and L_{\perp} lateral scale length). This is the typical collisional transport regime.¹⁰⁻¹² Furthermore, as is illustrated in Fig. 4, the resistivity of a compressed core is shown to be very small¹³ due to the relative high plasma temperature¹⁰ resulting from shock heating and capsule

compression; consequently, the interaction of the electron with dense plasma is well characterized by classical Coulomb collisions and the effects of the scattering will dominate the electron transport and energy deposition.

Thus a criterion for distinguishing the interaction regimes and for illustrating their relative importance ⁹ is approximately established based on above physics arguments as

$$\zeta \equiv \left. \frac{n_b}{n_e} \right|_{r_g = \lambda_D} = \frac{4\pi^2 t_b \sqrt{2m_e E^3}}{\mu_0^2 r_0 T_e \varepsilon_b}, \quad (2)$$

where r_0 is the classic electron radius. Figure 5 shows this ratio as a function of the beam energy for the case of 1 MeV electrons with $t_b=10$ ps in a DT plasma at 5 keV: when $n_b/n_e \geq \zeta$ the effects of self fields and associated instabilities are important, while when $n_b/n_e < \zeta$ the effects of classical Coulomb scattering are dominant.

We summarize and restate the above discussions from a different point of view in Fig. 6: when energetic electrons travel farther into the rapidly increased density portions of the capsule ($n_b/n_e < 10^{-2}$), Weibel-like instabilities⁷ are stabilized and the electrons are subject primarily to scattering processes. This stabilization can be understood since the gyro radius associated with the self-generated fields of the beam current is much larger than λ_D . Thus in this regime, the interaction can be envisioned as the linear superposition of individual, isolated electrons interacting with plasma.^{8,9} Hence these scattering processes, which involve energy loss, straggling and beam blooming, become the dominant mechanism that determines the details of energy deposition, whether in the dense core or outside, and therefore ultimately determine the effectiveness of capsule ignition.^{8,9}

III. THE MODEL OF ELECTRON ENERGY DEPOSITION

In the context of fast ignition, an analytic model^{8,9} has recently been developed to address the energy deposition of energetic electrons in the dense core. Country to previous work,¹⁴ this model rigorously treats the effects of the energy loss due to electron scattering and delineates the inextricable relationship of straggling and blooming with enhanced electron energy deposition. Specifically, the linear energy stopping power is given^{8,9}

$$\frac{dE}{dx} = \langle \cos \theta \rangle^{-1} \frac{dE}{ds} . \quad (3)$$

where dE/ds is plasma stopping power (continuous slowing down)

$$\frac{dE}{ds} = \frac{-2\pi r_0^2 m_0 c^2 n_i Z}{\beta^2} \left[\ln \left(\frac{(\gamma-1)\lambda_D}{2r_0\sqrt{2\gamma}} \right)^2 + 1 + \frac{1}{8} \left(\frac{\gamma-1}{\gamma} \right)^2 - \left(\frac{2\gamma-1}{\gamma} \right) \ln 2 + \ln \left(\frac{1.123\beta}{\sqrt{2kT_e/m_0c^2}} \right)^2 \right] \quad (4)$$

taken from Ref. 8, and

$$\langle \cos \theta \rangle = \exp \left(- \int_{E_0}^E \kappa_1(E') \left(\frac{dE'}{ds} \right)^{-1} dE' \right). \quad (5)$$

The effects of the scattering are manifested by the macroscopic transport cross sections of various orders (ℓ) which are all a function of the energy loss,

$$\kappa_\ell(E) = n_i \int \left(\frac{d\sigma}{d\Omega} \right) [1 - P_\ell(\cos \theta)] d\Omega . \quad (6)$$

In particular, when $\ell=1$,^{8,9}

$$\kappa_1(E) = 4\pi n_i \left(\frac{r_0}{\gamma\beta^2} \right)^2 \left[Z^2 \ln \Lambda^{ei} + \frac{4(\gamma+1)^2}{\left(2\sqrt{(\gamma+1)/2} \right)^4} Z \ln \Lambda^{ee} \right], \quad (7)$$

which relates to the slowing down cross section and characterizes the loss of directed velocity (momentum) in the scattering¹¹; and when $\ell=2$,⁹

$$\kappa_2(E) = 12\pi n_i \left(\frac{r_0}{\gamma\beta^2} \right)^2 \left[Z^2 \left(\ln \Lambda^{ei} - \frac{1}{2} \right) + \frac{4(\gamma+1)^2}{\left(2\sqrt{(\gamma+1)/2} \right)^4} Z \left(\ln \Lambda^{ee} - \frac{1}{2} \right) \right], \quad (8)$$

which relates to the deflection cross section and represents mean-square increment in the transverse electron velocity during the scattering process.¹¹ From Eq. (3), dE/dx is effectively enhanced over dE/ds due to the effects of the scattering ($\langle \cos \theta \rangle \leq 1$).

Furthermore, in our calculations, the longitudinal straggling is⁹

$$\Sigma_R(E) = \sqrt{\langle x^2 \rangle - \langle x \rangle^2}, \quad (9)$$

and the beam blooming is⁹

$$\Sigma_B(E) = \sqrt{\langle y^2 \rangle}, \quad (10)$$

(since azimuthal symmetry: $\langle y \rangle = \langle z \rangle = 0$). Both $\Sigma_R(E)$ and $\Sigma_B(E)$ are calculated by evaluating basic moments required for the calculation of the longitudinal and lateral distributions:

$$\langle x \rangle = \int_{E_0}^E \langle P_1(\cos \theta) \rangle \left(\frac{dE'}{ds} \right)^{-1} dE'; \quad (11)$$

$$\langle x^2 \rangle = \frac{2}{3} \int_{E_0}^E \langle P_1(\cos \theta) \rangle \left(\frac{dE'}{ds} \right)^{-1} \left(\int_{E_0}^{E'} \frac{1 + 2\langle P_2(\cos \theta) \rangle}{\langle P_1(\cos \theta) \rangle} \left(\frac{dE''}{ds} \right)^{-1} dE'' \right) dE'; \quad (12)$$

and

$$\langle y^2 \rangle = \langle z^2 \rangle = \frac{2}{3} \int_{E_0}^E \langle P_1(\cos \theta) \rangle \left(\frac{dE'}{ds} \right)^{-1} \left(\int_{E_0}^{E'} \frac{1 - \langle P_2(\cos \theta) \rangle}{\langle P_1(\cos \theta) \rangle} \left(\frac{dE''}{ds} \right)^{-1} dE'' \right) dE', \quad (13)$$

where

$$\langle P_\ell(\cos \theta) \rangle = \exp \left\{ - \int_{E_0}^E \kappa_\ell(E') \left(\frac{dE'}{ds} \right)^{-1} dE' \right\}. \quad (14)$$

Figure 7 shows both $\Sigma_R(E)$ and $\Sigma_B(E)$ as a function of electron energy loss $[\Delta E = (E_0 - E)/E_0]$ for 1-MeV electrons in a DT plasma ($\rho = 300/\text{cm}^3$, $T_e = 5$ keV). As a consequence of the effects of energy loss upon the scattering, it is shown that the energy deposition, towards the end of the penetration, is transferred to an extended region about the mean penetration of 13.9 μm , specifically $\sim \pm 3$ μm longitudinally and $\sim \pm 5$ μm laterally.⁹ Further illustrated in Fig. 8, the stopping power is now seen effectively enhanced in the extended region in which straggling and blooming are important. Such enhancement forms an effective ‘‘Bragg peak’’. In contrast, the traditional *electron* stopping Bragg peak^{15,16} occurs at energies ~ 50 eV or less for $Z=1$, which results solely from the velocity match between the incident electron and plasma electrons and included no scattering at all.¹⁷ The combined effects of blooming and straggling will result in an asymmetric energy deposition region about the mean penetration.⁹

Figure 9 further shows the details of the energy deposition in a compressed target. Notable is the fact that little straggling or blooming occurs until the 1-MeV electrons have traversed a significant portion of the final penetration ($\sim 60\%$, corresponding to only $\sim 40\%$ energy loss). We can see that the assumption of uniform energy deposition, used

in some previous calculations and also plotted in Fig. 9, has some approximate justification only for the first $\sim 40\%$ of the energy loss. For energy loss greater than 40% , both straggling and blooming expand linearly with the square root of the penetration, an effect associated with the enhanced energy loss of the effective Bragg peak. As a direct consequence of these multiple scattering effects, these results demonstrate the inextricably linkage between enhanced energy loss, straggling, and blooming.⁹

IV. DISCUSSIONS

To further delineate the basic features and applications of this model, the fundamental dependence of the scattering effects on plasma Z , density, temperature, and electron energy are discussed in this section. However, because of the non-linear coupling of energy loss, straggling, and blooming, as is reflected in the complex integrands and limits in the double and triple integrals [for example, Eqs. (11) - (14)], there is no simple analytic reduction for these results. Thus, we will evaluate these effects and their dependences, albeit numerically, in the context of the fast ignition.

A. Dependence of scattering on plasma Z

The strong Z -dependence of scattering is directly reflected in the penetration, blooming and straggling. To explicitly illustrate this, both $\langle x \rangle$ and Σ_B ($\Sigma_B / \langle x \rangle$) are evaluated numerically for $Z=1, 4, 13,$ and 29 , and the results are plotted in Fig. 10. For facilitating the comparison, we have assumed that these plasmas all have the same electron density ($n_e=7.2 \times 10^{25}$ and $T_e=5$ keV). With this assumption, the total path length ($R = \int_{E_0}^{T_e} (dE/ds)^{-1} dE$),^{8,9,18} which doesn't include at all the effects of scattering, should be identical for all these plasmas because energy loss to plasma electrons is the only mechanism for electron stopping. However, as shown in Fig. 10(a), including the effects of scattering significantly decreases the penetration. In particular, with increasing Z , the penetration, but not the total path length, rapidly drops and blooming effects ($\Sigma_B/\langle x \rangle$) notably increase [Fig. 10(a) and 10(b)]. This strong Z -dependence results directly from the macroscopic transport cross sections, Eqs. (7) and (8), where the scattering scale as Z^2 and will play an overwhelmingly dominant role for higher Z plasmas.

B. Dependence of scattering on plasma density

As illustrated in Fig. 11, the scattering effects ($\Sigma_R/\langle x \rangle$ and $\Sigma_B/\langle x \rangle$) and $\rho\langle x \rangle$ are insensitive to the plasma density. This insensitivity results from the effective cancellation of the density in these calculations. (For example, $\rho \propto n_i$ while $\langle x \rangle \propto n_i^{-1}$. The slight increase in $\rho\langle x \rangle$ with density simply reflects the slight decrease in the Coulomb logarithm of the stopping power as the density increases^{8,9}). The significance of these results is that the overall effect of the scattering is solely determined by the areal density that these electron travel through. Consequently, the plasma density gradients, such as would occur towards the core region of an actual fast ignition experiment, will not impact the general scope or the final results of these calculations.

C. Dependence of scattering on plasma temperature

The temperature dependence is shown to be weak; As illustrated in Fig. 12, a factor of 10 reduction in temperature results in only a $\sim 10\%$ reduction in the penetration. This is because the projectile electrons are so energetic compared to the background plasmas that plasma temperature dependence is weak.^{8,9} However, as the initial electron energy decreases, the effect of scattering becomes more pronounced (this is similar to what is seen in the scattering of energetic electrons in metals¹⁹). For a given electron energy, scattering effects slightly decrease as the target plasma temperature decreases, *i.e.* the path of an electron slightly straightens as the target plasma temperature drops. For example, when the target plasma temperature changes from 5.0 to 0.5 keV ($\rho=300$ g/cm³), the ratio $R/\langle X_p \rangle$ is reduced by $\sim 5\%$ for 1-MeV electrons.

D. Dependence of scattering on electron energy

Finally, the dependence of scattering on projectile electron energy is explicitly illustrated in Fig. 13: while electrons with higher energy penetrate farther, the scattering effects ($\Sigma_R/\langle x \rangle$ and $\Sigma_B/\langle x \rangle$) are significantly enhanced as the electron energy decreases from 10 to 0.1 MeV. These effects are also important for the electron preheat problem,^{20,21} even for regimes of lower energy and much lower density.

V. SUMMARY

In summary, we have analytically modeled the energy deposition of MeV electrons in dense plasmas in the context of ICF fast ignition. It is found that the effects of classical stopping and scattering dominate the electron transport and energy deposition in the region of dense plasmas. The calculations presented in this article rigorously treat the effects of the energy loss due to multiple electron scattering, as well as the effects of longitudinal straggling and transverse blooming, and their inextricable relationship with enhanced electron energy deposition. The penetration of 1-MeV electrons is reduced from 0.54 to 0.41 g/cm². In particular, it has been demonstrated that, while the initial penetration results in approximately uniform energy deposition, the latter penetration has mutual couplings of energy loss, straggling, and blooming that lead to an extended region of enhanced, non-uniform energy deposition. These results are critically important for quantitatively assessing ignition requirements of fast ignition.

ACKNOWLEDGMENTS

This work was supported in part by U.S. Department of Energy Contract #DE-FG03-99SF21782, LLE subcontract #PO410025G, LLNL subcontract #B313975, and the Fusion Science Center for Extreme States of Matter and Fast Ignition Physics at University of Rochester.

¹ M. Tabak, J. Hammer, M. Glinsky, W. L. Kruer, S. C. Wilks, J. Woodworth, E. M. Campbell, M. D. Perry, and R. J. Mason, *Phys. Plasmas* **1**, 1626 (1994).

² S. Atzeni, *Phys. Plasmas* **6**, 3316 (1999).

³ S. Atzeni and J. Meyer-Ter-Vehn, *The Physics of Inertial Fusion* (Clarendon, Oxford, 2004).

⁴ A. Pukhov and J. Meyer-Ter-Vehn, *Phys. Rev. Lett.* **76**, 3975 (1996).

⁵ M. Honda, J. Meyer-ter-Vehn and A. Pukhov, *Phys. Rev. Lett.* **85**, 2128 (2000).

⁶ L. Gremillet, G. Bonnaud, and F. Amiranoff, *Phys. Plasmas* **9**, 941 (2002).

⁷ E. S. Weibel, *Phys. Rev. Lett.* **2**, 83 (1959).

⁸ C. K. Li and R. D. Petrasso, *Phys. Rev.* **E. 70**, 067401 (2004).

⁹ C. K. Li and R. D. Petrasso, "Stopping, Straggling and Blooming of Directed Energetic Electrons in Hydrogenic and Arbitrary-Z Plasmas" submitted to *Phys. Rev.* **E.** (2005).

- ¹⁰ L. Spitzer, *Physics of Fully Ionized Gases* (Interscience, New York, 1962).
- ¹¹ B. Trubnikov, *Review of Plasma Physics* 1 (consultants Bureau, New York, 1965).
- ¹² S. I. Braginskii, *Review of Plasma Physics* 1 (consultants Bureau, New York, 1965).
- ¹³ H. M. Milchberg, R. R. Freeman, S. Davey, and R. More, *Phys. Rev. Lett.* **61**, 2368 (1988).
- ¹⁴ C. Deutsch, H. Furukawa, K. Mima and K. Nishihara, *Phys. Rev. Lett.* **77**, 2489 (1996). Erratum, *Phys. Rev. Lett.* **85**, 1140 (2000).
- ¹⁵ R. D. Evans, *The Atomic Nucleus* (McGraw-Hill, New York, 1955).
- ¹⁶ M. J. Berger and S. M. Seltzer, NAS-NRC Publication 1133 (1965); L. Pages *et al.*, *Atomic Data* **4**, 1-127 (1972), and references therein.
- ¹⁷ The traditional Bragg peak cannot be reflected in the “continuous slowing down calculations” since we integrate down to energy losses corresponding to 95% of the initial energy, which is well above this energy. This is of course in contrast to the *ion* Bragg peak, which occurs at energies of ~ 100 keV, and which is physically realizable in many circumstances and experiments.
- ¹⁸ C. K. Li and R. D. Petrasso, *Phys. Rev. Lett.* **70**, 3059 (1993).
- ¹⁹ K. H. Weber, *Nucl. Instrum. Methods* **25**, 261 (1964).
- ²⁰ M. D. Rosen, M. D. Rosen, R. H. Price, E. M. Campbell, D. W. Phillion, K. G. Estabrook, B. F. Lasinski, and J. M. Auerbach, S. P. Obenshain, E. A. McLean, R. R. Whitlock, and B. H. Ripin, *Phys. Rev. A* **36**, 247 (1987).
- ²¹ J. D. Lindl, *Inertial Confinement Fusion* (Springer, New York, 1998).

Fig. 1

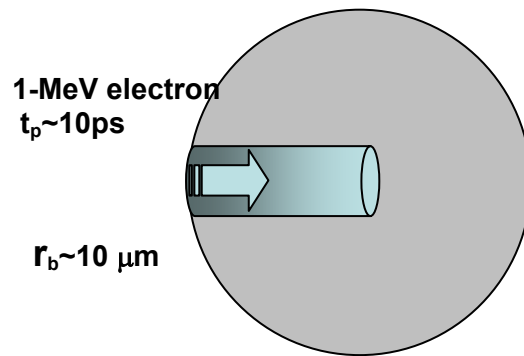


FIG. 1. The fast ignition scheme is schematically illustrated in this diagram: \sim MeV electrons generated by high intensity, shot-pulse laser at the critical surface need to transport to the pre-compressed target core. These electrons interact with, and deposit energy to, the background plasma whose density evolves from 10^{21} to 10^{26} /cm³. Typically, the electron beam has a pulse length \sim 10 ps and beam radius \sim 10 μ m.

Fig. 2

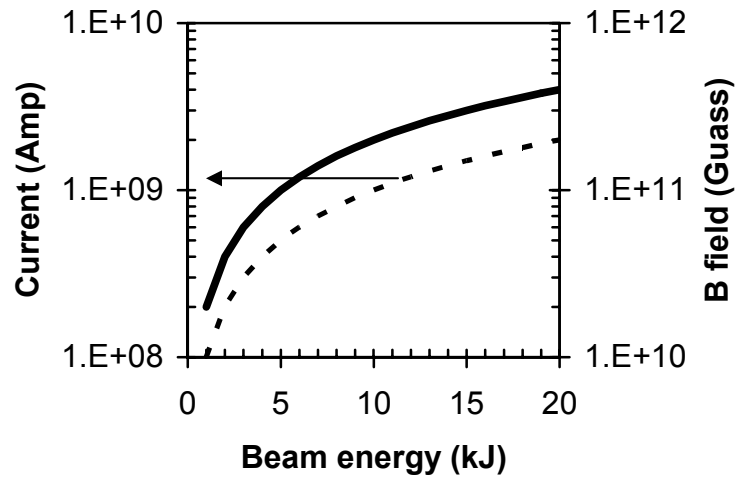


FIG. 2. The beam current I_b and associated B_{max} are plotted as a function of the beam energy ε_b , for $E=1$ MeV and $t_b=10$ ps, a typical case relevant to fast ignition.

Fig. 3

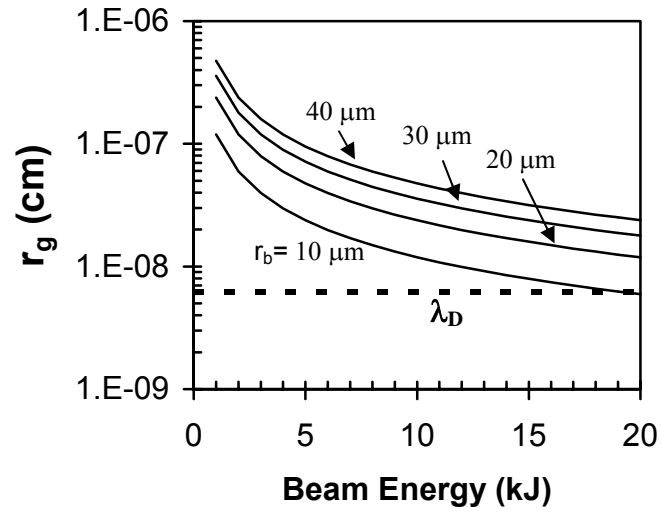


FIG. 3. The maximum electron gyroradius r_g as a function of beam energy for the cases where beam radius $r_b=10, 20, 30, 40 \mu\text{m}$, and the plasma Debye length λ_D in the compressed target (a DT plasma with $\rho=300 \text{ g/cm}^3$ and $T_e=5 \text{ keV}$). It is seen that for the cases we are considering r_g 's are all consistently larger than the λ_D . Only for very large energy deposition and very small deposition regions does r_g approach λ_D .

Fig. 4

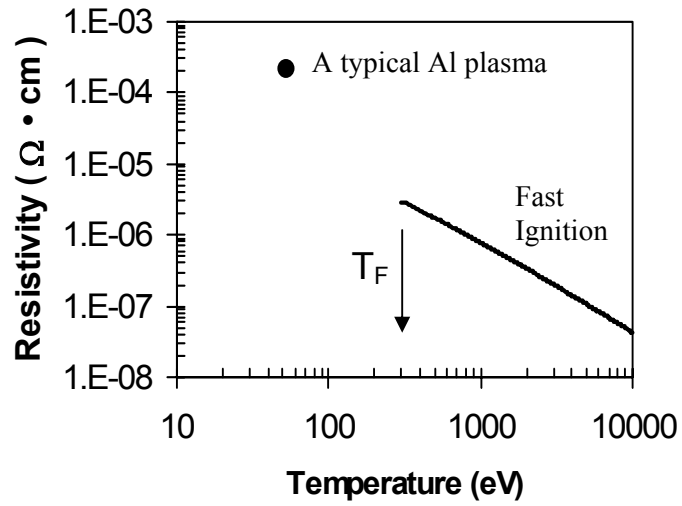


FIG. 4. The resistivity of a compressed core is shown to be several orders of magnitude smaller than that of a plasma generated by a short pulse laser on a solid target such as Al (for which case the resistivity plays an important role in plasma heating).¹³

Fig. 5

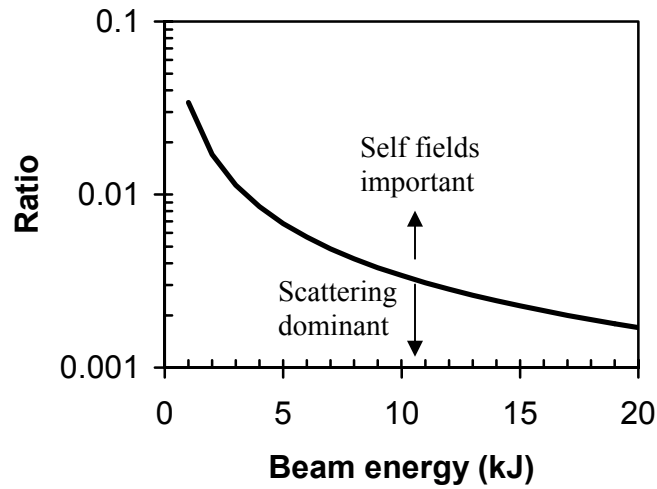


FIG. 5. The ratio defined by Eq. (2) is plotted as a function of the beam energy for the case of 1-MeV electrons with $t_b=10$ ps in plasma at 5 keV: when $n_b/n_e \geq \zeta$ the effects of self fields and associated instabilities are important while when $n_b/n_e < \zeta$ the effects of classical Coulomb scattering are dominant. It is the later that the ignition occurs and the ignition conditions are determined.^{8,9}

Fig. 6

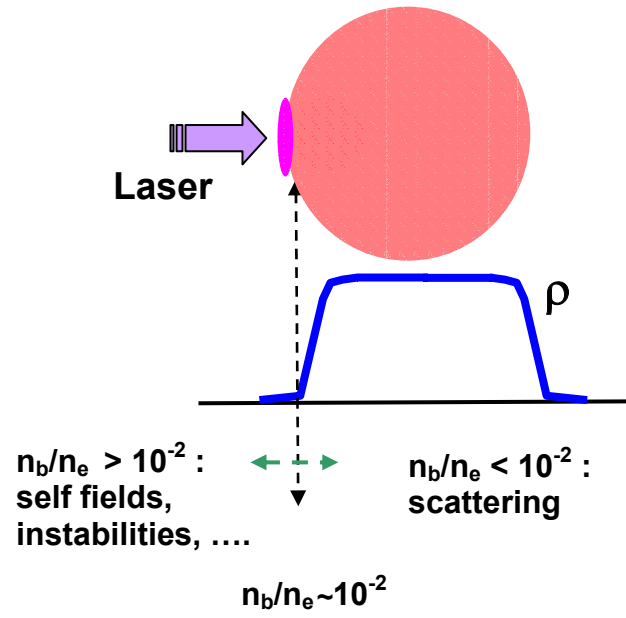


FIG. 6. Schematic illustration of MeV electron transport and energy deposition in a pre-compressed target. Two distinct regions for electron transport are illustrated: First, when $n_b/n_e > 10^{-2}$, electron transport is highly filamented due to Weibel-like instabilities which dominate energy loss and beam blooming; however, for $n_b/n_e < 10^{-2}$, for which λ_D is clearly smaller than the energetic electron gyro radius associated with the beam current, the Weibel-like instabilities⁷ are stabilized and the electrons are then subject to the scattering, straggling, and blooming processes described herein.^{8,9}

Fig. 7

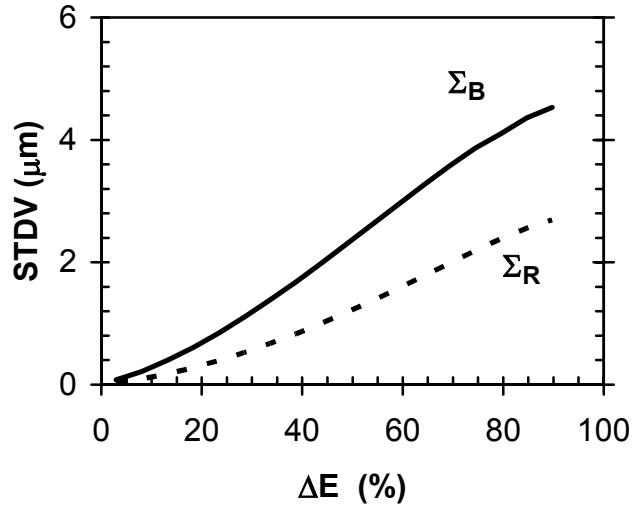


FIG. 7. The calculated range straggling $\Sigma_R(E)$ and beam blooming $\Sigma_B(E)$ as a function of electron residual energy for 1-MeV electrons in a DT plasma ($\rho=300/\text{cm}^3$, $T_e=5$ keV).

Fig. 8

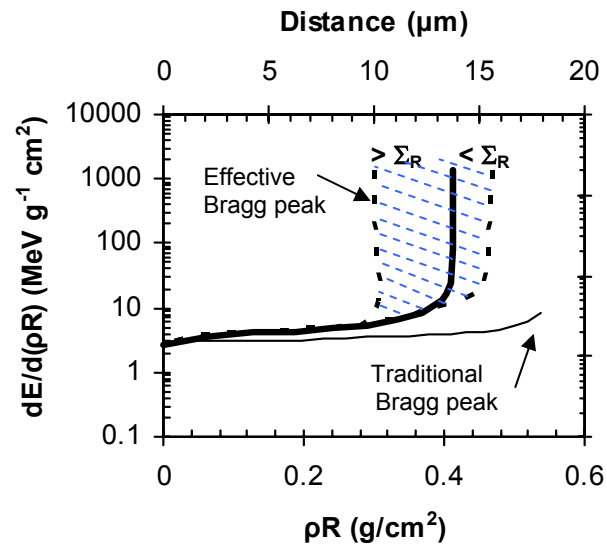


FIG. 8. The stopping power plotted as a function of the electron penetration for 1-MeV electrons in a DT plasma ($\rho=300\text{g/cm}^3$ and $T_e=5\text{ keV}$). The heavy solid line represents the mean energy loss, while the two dashed lines schematically indicate the straggling range over which energy is effectively spread.⁹ The thin line illustrates the continuous slowing-down approximation,¹⁵⁻¹⁷ and is directly related to R , the total path length.

Fig. 9

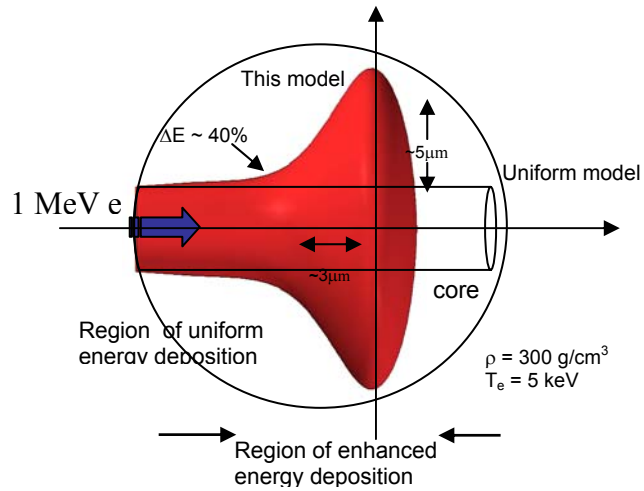


FIG. 9. Schematic illustration of the energy deposition profile for 1-MeV electrons in a DT plasma of 300 g/cm^3 at 5 keV. After considering the mutual coupling between stopping, straggling and blooming, we find that the energy deposition towards the end of the penetration occurs in an extended, non-uniform region about the mean penetration of $13.8 \mu\text{m}$, specifically $\sim \pm 5 \mu\text{m}$ laterally, and longitudinally $> 3 \mu\text{m}$ in the backward direction and $< 3 \mu\text{m}$ in the forward direction.

Fig. 10

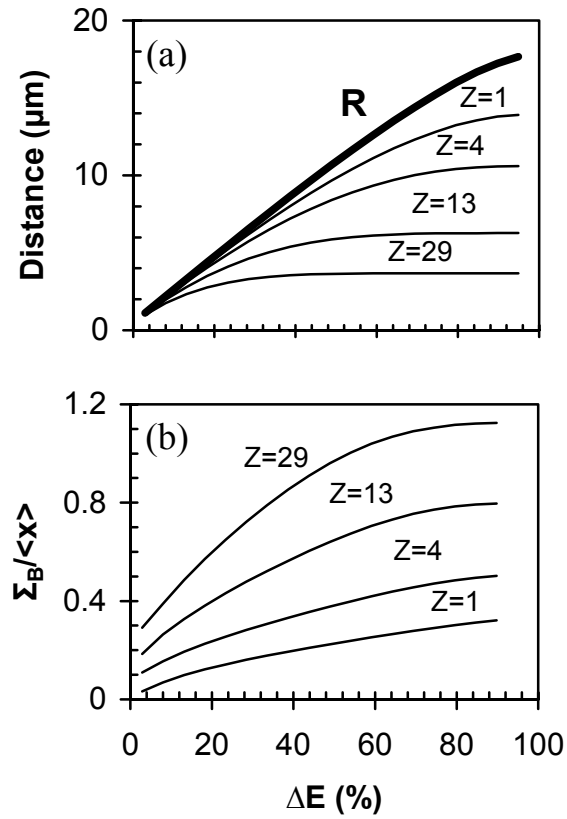


FIG. 10. The total path length (R), penetration ($\langle x \rangle$) and blooming ($\Sigma_B / \langle x \rangle$) are evaluated for interactions of 1 MeV electrons with DT, beryllium, aluminum and copper plasmas, assuming plasma $T_e = 5$ keV and $n_e = 7.2 \times 10^{25}$ in every cases. For Cu plasma, bremsstrahlung losses are about 5%, and are ignored.

Fig. 11

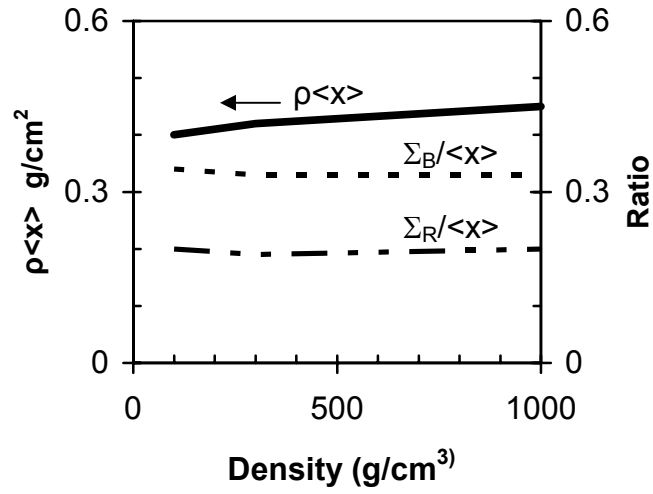


FIG.11. The scattering effects ($\Sigma_{R/\langle x \rangle}$ and $\Sigma_{B/\langle x \rangle}$) and the areal density ($\rho_{\langle x \rangle}$) for 1 MeV electrons in DT plasmas, plotted as a function of the plasma density. The dependence of scattering are shown to be relative insensitive to the densities in this regime.^{8,9}

Fig. 12

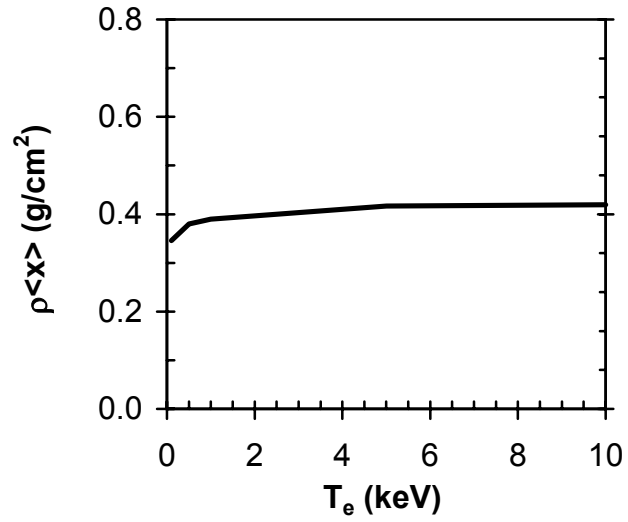


FIG. 12 The calculated penetration of 1-MeV electrons as a function of plasma temperature in a DT plasmas with $\rho=300\text{g/cm}^3$. It is seen that $\rho\langle x \rangle$ is relatively insensitive to plasma temperature.

Fig. 13

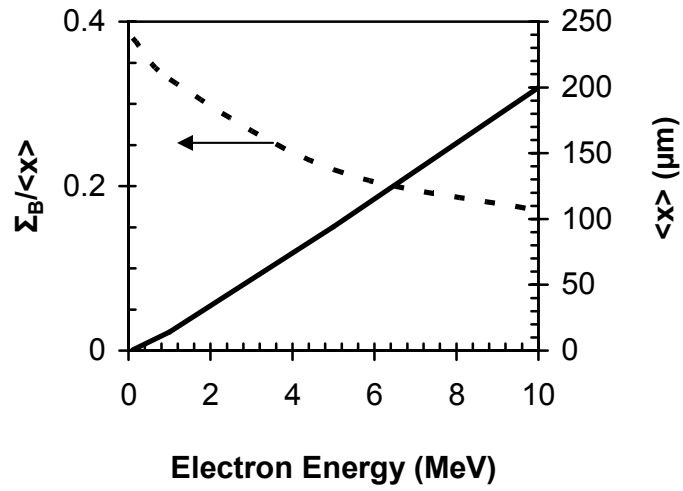


FIG. 13. Illustration of the enhancement of scattering effects ($\Sigma_R/\langle x \rangle$ and $\Sigma_B/\langle x \rangle$), as well as the electron penetration, as the electron energy decreases from 10 to 0.1 MeV in a DT plasma of $300\text{g}/\text{cm}^3$ at 5 keV.